Optimized Factor Graph for Tightly-Coupled LiDAR/IMU Localization in Underground Parking Garages

Wangyusha Bao[1], Jian Wang[1], Houzeng Han[1], Yiwen Zhao[1],Menghan Liu[1], He Wu [1]

[1] School of Geomatics and Urban Spatial Informatics, Beijing University of Civil Engineering and Architecture, 102616 Beijing,China - 18985431304@163.com,wangjian@bucea.edu.cn,hanhouzeng@bucea.edu.cn,2577274058@qq.com,liumenghan_0516@163.com,2546771391@qq.com

Keywords: LiDAR-SLAM, Underground Parking, Automatic Parking, IESKF, Graph Optimization.

Abstract

To address the challenge of intelligent vehicle localization in underground parking structures due to the loss of GNSS signals, this paper introduces a method to address this issue by developing a novel localization framework known as GF-LIO, which denotes a tightly-coupled fusion of LiDAR and IMU data, innovatively combining the Interactive Extended State Kalman Filter (IESKF) with a factor graph to enhance the localization process and solve the problem of GNSS signal loss in underground parking lots. The GF-LIO model commences with a strategic feature selection process, facilitated by a greedy algorithm that prioritizes environmental cues within the point cloud data. This method effectively filters out redundant features, thereby enhancing the saliency of retained features and subsequently improving the robustness of the localization process. Following feature selection, the model integrates LiDAR and IMU measurements utilizing the IESKF algorithm, ensuring a cohesive fusion of sensor data and bolstering attitude estimation accuracy. The culmination of the GF-LIO framework involves factor graph optimization, a sophisticated technique that synthesizes LiDAR odometry, IMU pre-integration factors, and loop closure detection factors. This optimization step enhances the overall precision and consistency of the localization process, resulting in superior performance compared to existing methodologies. Experimental evaluations conducted within underground parking environments corroborate the efficacy of the GF-LIO model. Comparative analyses against established approaches such as A-LOAM, LeGO-LOAM, LIO-LOAM, and FAST-LIO demonstrate a notable performance improvement exceeding 12.53%. The proposed model adeptly integrates domain-specific environmental characteristics with multi-sensor data, thereby facilitating precise localization and map construction tasks for intelligent vehicle navigating within the intricate confines of subterranean parking structures.

1. Introduction

Precise localization technology is crucial for enabling autonomous driving assistance systems, particularly in navigating complex urban environments. Current outdoor garage automatic parking systems typically rely on Inertial Measurement Unit (IMU) assistance alongside Global Navigation Satellite System (GNSS) to ensure continuous and reliable positioning, mitigating the challenges posed by GNSS accuracy degradation due to multipath effects in urban settings (Lategahn and Stiller, 2014;Ahmed et al., 2018). However, underground parking lots present a unique challenge as GNSS signals are inaccessible, necessitating alternative indoor positioning methods such as Bluetooth (Faragher and Harle, 2015), Wi-Fi (Yang and Shao, 2015), and Ultra-Wideband (UWB) (Li et al., 2009). Nevertheless, these methods often entail high deployment and maintenance costs due to the requirement for base stations, limiting their applicability in intelligent vehicle positioning systems. Consequently, improving navigation and positioning accuracy in underground parking scenarios remains imperative.

Simultaneous Localization and Mapping (SLAM) technology, leveraging cameras and LiDAR as primary sensors, offers a promising solution by enabling concurrent localization and scene model reconstruction. This approach facilitates the creation of a three-dimensional spatial framework within enclosed underground parking lots, providing real-time and robust support for safe automatic parking operations (Li et al., 2024). For instance, A global semantic map has been developed by detecting road instances such as curves and speed bumps in parking lots, with this information being integrated with wheel encoder data for precise positioning(Yan et al., 2021) . However, visual features are susceptible to variations in environmental lighting conditions, and their accuracy relies on the availability of sufficient landmarks. Many researchers have thus turned to LiDAR-based SLAM methods for underground parking lot positioning. An Inertia-Enhanced Generalized Iterative Closest Point (G-ICP) method(Li et al., 2018) was utilized, leveraging a multi-state Extended Kalman Filter to loosely couple LiDAR with IMU for the collaborative positioning of multiple vehicles in parking lots. Similarly,Parametric maps were constructed using horizontal and vertical geometric parameters and integrated into an online filter to estimate map parameters and localize vehicles within indoor parking lots(Han et al., 2018).

Although LiDAR-SLAM positioning methods for automatic parking systems in underground garages are an active area of research, existing LiDAR-inertial fusion approaches require further refinement to adapt to the unique challenges of underground parking environments and enhance automatic parking accuracy. Challenges include managing large data volumes and achieving real-time performance in multi-source data fusion, addressing robustness issues during vehicle manoeuvring within parking lots, and improving feature matching precision. To tackle these challenges, this paper proposes a factor graph-optimized LiDAR/IMU tightly-coupled Integrated Enhanced State Kalman Filter (IESKF) fusion model named GF-LIO for underground parking lot entry positioning. Initially, the model identifies and discards degraded point cloud features from the underground parking environment while retaining high-quality features to reduce redundancy. Subsequently, the IESKF algorithm is employed for tight LiDAR/IMU coupling to enhance attitude estimation robustness. Finally, through the integration of IMU pre-integration factors and loop closure detection factors, factor graph optimization updates LiDAR odometry pose, thereby improving overall positioning accuracy and consistency. This approach effectively integrates environmental characteristics of underground parking lots, consolidates multi-sensor data, and enhances pose estimation precision and stability.

2. Methodology

The overall framework of the GF-LIO model is depicted in Figure 1. This model is designed to achieve precise localization in challenging environments such as underground parking garages. It consists of several essential components, including data preprocessing, Integrated Enhanced State Kalman Filter (IESKF) odometry, factor graph global pose optimization, and loop closure detection. The front-end laser-inertial odometry relies on the tight coupling of IESKF, while the back end integrates various factors using a factor graph. The key steps involved in the GF-LIO model are outlined as follows:

1. Data Collection and Preprocessing: Utilize collected IMU acceleration and gyroscope data to estimate the vehicle's motion state and correct LiDAR point cloud distortion caused by vehicle motion through IMU pre-integration.

2. High-Quality Feature Extraction: Extract line and plane features from the point cloud based on curvature and identify degenerate features according to the feature vector. Replace degenerate features with predicted values and update features to obtain high-quality features.

3. Submap Update: Extract keyframes and construct submaps, conduct feature matching between frames and maps, and compute relative pose transformations.

4. IMU-LiDAR Tight Coupling Localization Based on IESKF: Fuse IMU and LiDAR observation data using IESKF to update the system state and output laser-inertial odometry pose factors.

5. Factor Graph Optimization: Select a keyframe-based Euclidean distance method for loop closure detection and jointly optimize IMU pre-integration factors and laser-inertial odometry factors within the sliding window during the same time segment as the keyframe to achieve the best estimation of the vehicle's pose state.

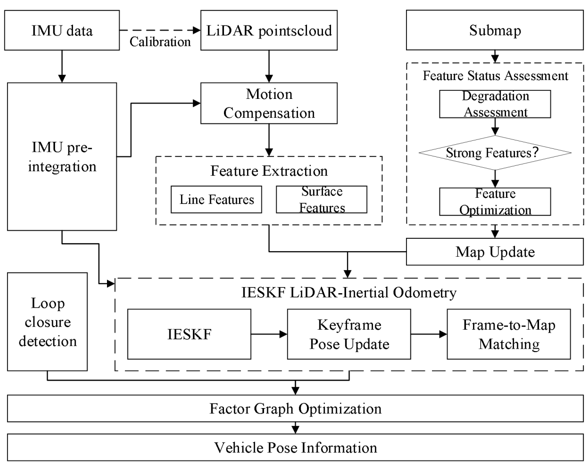

Figure 1. Overall Framework of the GF-LIO Model.

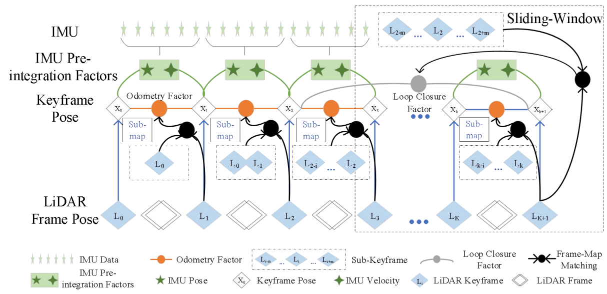

Figure 2. Factor Graph Model.

2.1 Vehicle Motion Model

In addressing vehicle motion in urban underground parking garage scenarios, we consider the presence of curved trajectories with slow speeds. Therefore, we adopt the Constant Turn Rate and Velocity (CTRV) model from the quadratic motion model. The CTRV model assumes that the vehicle moves along a straight path with constant turn rate and constant velocity. The schematic diagram of this model is provided below:

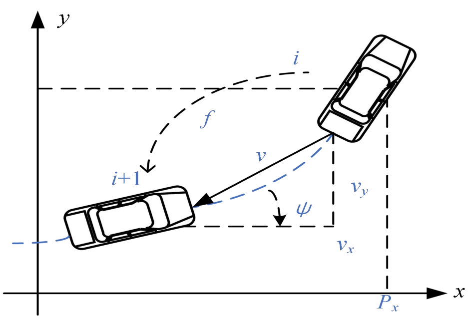

Figure 3. The CTRV model.

The state variables x of the vehicle can be represented as follows:

$$x = [p_x, p_y, v, \psi, \psi^{\cdot}]^T \tag{1}$$

The components of the equation represent the vehicle's position, velocity, yaw angle, and yaw rate in a two-dimensional plane. Discretizing the state variables over continuous time yields the state function in discrete time:

$$x_{k+1} = x_k + \begin{bmatrix} \frac{v_k}{\psi_k^{\cdot}}\left(\sin\left(\psi_k + \psi_k^{\cdot}\Delta t\right) - \sin\left(\psi_k\right)\right) \\ \frac{v_k}{\psi_k^{\cdot}}\left(-\cos\left(\psi_k + \psi_k^{\cdot}\Delta t\right) + \cos\left(\psi_k\right)\right) \\ 0 \\ \dot{\psi}_k \Delta t \\ 0 \end{bmatrix} \tag{2}$$

where, $\Delta t = t_{i+1} - t_i$ .When the vehicle is in a straight-line driving state, The state function of yaw rate $\psi_k^{\cdot} = 0$ can be expressed as:

$$x_{k+1} = x_k + \begin{bmatrix} v_k \cos(\psi)\Delta t \\ v_k \sin(\psi)\Delta t \\ 0 \\ 0 \\ 0 \end{bmatrix} \tag{3}$$

Taking into account the presence of noise errors during vehicle motion, we introduce straight-line acceleration noise v_a and yaw angle angular acceleration noise $v_{\ddot{\psi}}$ in the CTRV model all follow a Gaussian distribution with a mean of zero, $v_a \sim \mathcal{N}\left(0,\sigma_a^2\right), v_{\ddot{\psi}} \sim \mathcal{N}\left(0,\sigma_{\ddot{\psi}}^2\right)$ .So the state function with noise can be expressed as:

$$\mathrm{x}_{k+1} = \mathrm{x}_k + \begin{bmatrix} \frac{\mathrm{v}_k}{\psi_k^{\bullet}}\left(\sin\left(\psi_k + \psi_k^{\bullet}\Delta \mathrm{t}\right) - \sin\left(\psi_k\right)\right) \\ \frac{\mathrm{v}_k}{\psi_k^{\bullet}}\left(-\cos\left(\psi_k + \psi_k^{\bullet}\Delta \mathrm{t}\right) + \cos\left(\psi_k\right)\right) \\ 0 \\ \psi_k^{\bullet}\Delta \mathrm{t} \\ 0 \end{bmatrix} + \begin{bmatrix} \frac{1}{2} v_{a,k}\cos\left(\psi_k\right)(\Delta t)^2 \\ \frac{1}{2} v_{a,k}\sin\left(\psi_k\right)(\Delta t)^2 \\ v_{a,k}\Delta t \\ \frac{1}{2} v_{\ddot{\psi}}(\Delta t)^2 \\ v_{\ddot{\psi}}\Delta t \end{bmatrix} \tag{4}$$

2.2 Laser Point Cloud Feature Processing Model

The feature processing model is based on the unique linear and planar environmental characteristics of underground parking lots. It involves extracting point cloud features, processing feature degradation, enhancing high-quality features, optimizing degraded features, and improving the utilization rate of point cloud features.

2.2.1 Point Cloud Preprocessing: Point cloud data preprocessing primarily addresses the offset in point cloud data caused by high-speed movement and speed bump disturbances of vehicles in underground parking lots. Assuming the vehicle is moving at a constant speed, high-frequency IMU data is used to perform linear interpolation on the point cloud, transferring the rotation quantity of the IMU between adjacent frames, and removing motion distortion through transformation matrices. Define the inertial coordinate system *I*, the LiDAR coordinate system *L*, and the laser-inertial odometry coordinate system *O*。Assuming that the acceleration and, angular velocity at time *t* between the start time *i* and end time *j* of the current laser point cloud frame are constant and unchanged $\left(t = i, i+1, ..., j\right)$,The LiDAR frames corresponding to the start and end times are denoted as L_i and L_j .Integrating the IMU measurements between these two frames yields the corresponding estimated quantity $\boldsymbol{x}_{I_t}^{O}$.

$$\boldsymbol{x}_{I_t}^{O} = \left[\boldsymbol{p}_{I_t}^{O} \quad \boldsymbol{v}_{I_t}^{O} \quad \boldsymbol{q}_{I_t}^{O} \quad \boldsymbol{b}_{a_t}^{\mathrm{T}} \quad \boldsymbol{b}_{g_t}^{\mathrm{T}}\right]^{\mathrm{T}} \tag{5}$$

$$\begin{cases} \boldsymbol{p}_{I_j}^{O} = \boldsymbol{p}_{I_i}^{O} + \sum_{t=i}^{j-1}\left(\boldsymbol{v}_{I_t}^{W}\Delta t + \frac{1}{2}\left(\boldsymbol{R}_t^{W}\left(\hat{\boldsymbol{a}}_t - \boldsymbol{b}_{a_t}\right) - \boldsymbol{g}^{O}\right)\Delta t^2\right) \\ \boldsymbol{v}_{I_j}^{O} = \boldsymbol{v}_{I_i}^{O} + \sum_{t=i}^{j-1}\left(\boldsymbol{R}_t^{O}\left(\hat{\boldsymbol{a}}_t - \boldsymbol{b}_{a_t}\right) - \boldsymbol{g}^{O}\right)\Delta t \\ \boldsymbol{q}_{I_j}^{O} = \boldsymbol{q}_{I_j}^{O} \otimes \prod_{t=i}^{j-1}\left(\begin{bmatrix} \frac{1}{2}\left(\hat{\boldsymbol{\omega}}_t - \boldsymbol{b}_{\omega_t}\right)\Delta t \\ 1 \end{bmatrix}\right) \end{cases} \tag{6}$$

Where $\boldsymbol{p}_{I_t}^{O}$, $\boldsymbol{v}_{I_t}^{O}$, $\boldsymbol{q}_{I_t}^{O}$ represent the position, velocity, and orientation in the world coordinate system at time *t*, respectively ; $\boldsymbol{g}^{O}$ a represents the gravitational acceleration in the laser-inertial odometry coordinate system; $\boldsymbol{R}_t^{W}$ and $\boldsymbol{R}_t^{O}$ represent the rotation matrices from the world coordinate system to the laser-inertial odometry coordinate system at time *t*. Based on the variations of the extrinsic parameters $\boldsymbol{T}_I^L$ between the IMU and the LiDAR, the pose $\boldsymbol{T}_j^i$ at time *j* relative to time *i* can be calculated through interpolation. Once the coordinate systems are aligned, the point cloud distortion correction is completed.

$$\boldsymbol{T}_I^L = \left[\boldsymbol{p}_I^{L\mathrm{T}} \quad \boldsymbol{q}_I^{L\mathrm{T}}\right]^{\mathrm{T}} \tag{7}$$

$$\boldsymbol{T}_j^i = \boldsymbol{T}_i^{\omega^{-1}}\boldsymbol{T}_j^{\omega} \tag{8}$$

2.2.2 Selection of High-Quality Features: environment features are assessed, and a random greedy algorithm is applied to dynamically optimize the feature information matrix and adjust the feature count. These transforms feature selection into a combinatorial optimization problem under technical information constraints, actively selecting appropriate feature subsets to enhance the accuracy and efficiency of the SLAM system. Assuming that point p_i and its five adjacent points in the same vertical direction form a point set *S*, compute the curvature of point p_i :

$$c = \frac{1}{|S|\left\|\boldsymbol{r}_i\right\|}\sum_{j\in S, j\neq i}\left\|\left(\boldsymbol{r}_j - \boldsymbol{r}_i\right)\right\| \tag{9}$$

Given a smoothness threshold c_{th} , if the smoothness is greater than the threshold, the point cloud is considered as an edge point, forming the edge point set F_e , otherwise, it is considered as a planar point, forming the planar point set F_p . To improve efficiency, a certain number of planar points and edge points are extracted to form a new point set. Assuming the feature point cloud set at time t $\left(t = i, i+1, ..., j\right)$ is $\left\{F_e^t, F_{me}^t, F_p^t, F_{mp}^t\right\}$, where $F_{me} \subset F_e, F_{mp} \subset F_p$, each F_{me} contains two edge points, and each F_{mp} contains four planar points. Through selecting an edge point p_j in F_e^j ,the nearest point p_i in F_e^j to p_j based on KD-Trees determined, along with the point p_n nearest to p_i among the adjacent laser beams, ensuring that the three points are not collinear. The association equation of this edge point is represented by the distance from the point to the line:

$$d_L = \frac{\left|\left(\boldsymbol{X}_{(j,p_j)}^L - \boldsymbol{X}_{(i,p_i)}^L\right)\times\left(\boldsymbol{X}_{(j,p_j)}^L - \boldsymbol{X}_{(i,p_n)}^L\right)\right|}{\left|\boldsymbol{X}_{(i,p_i)}^L - \boldsymbol{X}_{(i,p_n)}^L\right|} \tag{10}$$

Where $\boldsymbol{X}_{(i,p_j)}^L$ represents the line feature coordinates corresponding to the *j-th* frame, and $\boldsymbol{X}_{(i,p_i)}^L$, $\boldsymbol{X}_{(i,p_n)}^L$ represent the line feature coordinates corresponding to the *i-th* frame. Similarly, the association equation for plane points can be constructed, representing the distance from the point to the plane:

$$d_h = \frac{\left|\left(\left(\boldsymbol{X}_{(j,j)}^h - \boldsymbol{X}_{(i,i)}^h\right)\times\left(\boldsymbol{X}_{(i,i)}^h - \boldsymbol{X}_{(i,n)}^h\right)\times\left(\boldsymbol{X}_{(i,i)}^h - \boldsymbol{X}_{(i,m)}^h\right)\right)\right|}{\left|\left(\boldsymbol{X}_{(i,i)}^h - \boldsymbol{X}_{(i,n)}^h\right)\times\left(\boldsymbol{X}_{(i,i)}^h - \boldsymbol{X}_{(i,m)}^{h)}\right)\right|} \tag{11}$$

Where $\boldsymbol{X}_{(j,j)}^{h}$ represents the surface feature coordinates corresponding to the *j-th* frame, $\boldsymbol{X}_{(i,i)}^{h}$, $\boldsymbol{X}_{(i,n)}^{h}$ and $\boldsymbol{X}_{(i,m)}^{h)}$ represent the surface feature coordinates corresponding to the *i-th* frame. To assess the quality of features, let $N = |F_K|$ denote the total number of features, M denote the maximum number of selected features S_K , represent the set of high-quality features, and $f(\bullet)$ denote the mechanism measuring feature attributes. The feature selection formula based on parameter constraints is expressed as:

$$\arg\max_{S_K \subset F_K} f\left[\Lambda\left(S_K\right)\right] \text{subject to } |S_K| \le M \tag{12}$$

Where $\Lambda(S_K)$ represents the information matrix of the set of high-quality features. $f(\Lambda): tr(\Lambda)$ denotes the trace of the matrix, $\lambda_{\min}(\Lambda)$ denotes the minimum eigenvalue, and $\log\det(\Lambda)$ represents the logarithmic determinant used as a metric indicator for adaptively changing M。

To find high-quality features in real-time, a random greedy algorithm is employed to improve search efficiency. A subset of randomly sampled points from the map associated with the current frame is selected, and the residuals of all features in the subset are computed to choose the optimal feature. Subsequently, updates are made to the three information matrices in the algorithm. The loop terminates when the computation time for selecting high-quality features exceeds t_{MAX} or exceeds the maximum allowable number of high-quality features. The size of the random subset is defined as $\frac{N}{M}\log\left(\frac{1}{\varepsilon}\right)$, where ε is the degeneracy factor. The time complexity is $O\left(N\log\left(\frac{1}{\varepsilon}\right)\right)$, independent of *M*. Assuming $f(\bullet)$ is a non-negative monotonic submodular function, the size of the random subset is set to $\frac{N}{M}\log\left(\frac{1}{\varepsilon}\right)$. S_K^{*} represents the optimal set, and $S_K^{\#}$ is the result of the random greedy algorithm. The expected approximation of $S_K^{\#}$ is:

$$\mathrm{E}\left(f\left[\boldsymbol{\Lambda}\left(S_K^{\#}\right)\right]\right) \ge \underbrace{\left(1-1/e-\varepsilon\right)}_{\text{expected ratio}} f\left[\boldsymbol{\Lambda}\left(S_K^{*}\right)\right] \tag{13}$$

Finally, based on the logarithm of the determinants computed from all feature sets, it is determined whether they are high-quality features, and the map state is updated using these high-quality features.

2.3 Coupled Localization Model Based on IESKF

An a priori map is established based on the LiDAR to determine the vehicle's pose information in the underground parking garage, and during the parking process, the pose is updated by matching frames to the map. In this paper, the IESKF is employed to achieve tight coupling between LiDAR and IMU. Compared to traditional Kalman filtering, this model utilizes a real-time linearized system, where the first-order partial derivative of the error state is closer to the true state. Moreover, during the optimization process, the error rotation variable is approximated to zero, avoiding gimbal lock phenomena, reducing computational complexity, and minimizing errors. The overall framework is proposed based on LINS(Qin et al. ,2019) and FAST-LIO1(Xu et al., 2021), mainly divided into the following parts:

(1) Observation State Prediction: Assuming the system state variables $\breve{\boldsymbol{x}}_i = \left[\boldsymbol{p}^{\mathrm{T}}, \boldsymbol{q}^{\mathrm{T}}, \boldsymbol{v}^{\mathrm{T}}, \boldsymbol{b}_g^{\mathrm{T}}, \boldsymbol{b}_a^{\mathrm{T}}, \boldsymbol{g}^{\mathrm{T}}\right]^{\mathrm{T}}$ represent the pose change from the *i-th+1* frame data to the *i-th* frame data, including displacement, rotation, velocity, gyroscope bias, accelerometer bias, and gravity. Inputting the motion-compensated LiDAR point cloud, IMU measurements, and measurement noise $\boldsymbol{u}_i, \boldsymbol{\omega}_i$, with $\boldsymbol{\omega}_i = 0$, predicts the state variable $\breve{\boldsymbol{x}}_i$ to obtain the next moment's state variable $\breve{\boldsymbol{x}}_{i+1}$:

$$\breve{\boldsymbol{x}}_{i+1} = \breve{\boldsymbol{x}}_i \oplus \left[\mathrm{f}\left(\breve{\boldsymbol{x}}_i, \boldsymbol{u}_i, \boldsymbol{\omega}_i\right) \cdot \Delta t\right] \tag{14}$$

$$\breve{\boldsymbol{P}}_{i+1} = \boldsymbol{F}_i \breve{\boldsymbol{P}}_i \boldsymbol{F}_i^{\mathrm{T}} + \boldsymbol{B}_i \boldsymbol{Q} \boldsymbol{B} \boldsymbol{B}_i^{\mathrm{T}} \tag{15}$$

In equation (14), $\oplus$ denotes the generalized addition, $f\left(\breve{x}_i, \boldsymbol{u}_i, \boldsymbol{\omega}_i\right)$ represents the state transition matrix that projects the state change of the system variables between two consecutive LiDAR frames at times i and i+1, based on the measurement error state. Δt is the IMU sampling period. In equation (15), $\breve{\boldsymbol{P}}_{i+1}$ represents the predicted covariance matrix at time *i+1*, $\boldsymbol{F}_i$ is the predicted state matrix at time *i*, $\boldsymbol{B}_i$ is the noise matrix, $\boldsymbol{Q}$ is the noise covariance matrix. After each iteration, the absolute difference between the state variables and the previous predicted values is checked to see if it is smaller than a threshold value σ:

$$\left\|\breve{x}_{i+1}^{\alpha+1} \ominus \breve{x}_{i+1}^{\alpha}\right\| < \sigma \tag{16}$$

If it is less than the threshold, then the Jacobian matrix at the error state vector $\delta\boldsymbol{x}_{i+1} = 0$ for the *i+1* frame is computed, $\boldsymbol{A}_{i+1}\left(\delta\boldsymbol{\theta}_{i+1}\right) = I - \frac{1}{2}\delta\boldsymbol{\theta}$ represents the rotational part of the matrix that describes the change in the error state between the updated state and the previous state. Equation (18) is used to update the prior covariance matrix:

$$\begin{gathered}\delta\boldsymbol{x}_{i+1} = \breve{\boldsymbol{x}}_{i+1}^{\alpha+1} \ominus \breve{\boldsymbol{x}}_{i+1}^{\alpha} + \boldsymbol{J}_{i+1}^{\alpha}\delta\boldsymbol{x}_{i+1}^{\alpha} \\ \boldsymbol{J}_{i+1}^{\alpha} = \begin{bmatrix} \boldsymbol{A}_{i+1}\left(\delta\boldsymbol{\theta}_{i+1}\right)^{-\mathrm{T}} & 0 \\ 0 & \boldsymbol{I} \end{bmatrix}\end{gathered} \tag{17}$$

$$\breve{\boldsymbol{P}}_{i+1} = \left(\boldsymbol{J}_{i+1}^{\alpha}\right)^{-1} \breve{\boldsymbol{P}}_{i+1} \left(\boldsymbol{J}_{i+1}^{\alpha}\right)^{-\mathrm{T}} \tag{18}$$

(2) Error State Update: Based on the pose changes of adjacent frames $\boldsymbol{x}_{i+1}$ as in equation (14), residual equations $f\left(\boldsymbol{X}_{i+1}^{i}\right)$ of observation values are introduced. Covariance matrices H_{i+1} are calculated for both the edge point set and the plane point set:

$$f\left(\boldsymbol{X}_{i+1}^{i}\right) = \begin{cases} \dfrac{\left|\left(\tilde{\boldsymbol{X}}_{(i+1,i)}^{me} - \boldsymbol{X}_{(i+1,i)}^{me}\right) \times \left(\tilde{\boldsymbol{X}}_{(i+1,i)}^{me} - \boldsymbol{X}_{(i,l)}^{me}\right)\right|}{\left|\boldsymbol{X}_{(i,j)}^{Le} - \boldsymbol{X}_{(i,l)}^{Le}\right|} & \text{edge points} \\ \dfrac{\left|\left(\tilde{\boldsymbol{X}}_{(i+1,i)}^{mp} - \boldsymbol{X}_{(i,j)}^{mp}\right)\left(\left(\boldsymbol{X}_{(i,j)}^{mp} - \boldsymbol{X}_{(i,l)}^{mp}\right) \times \left(\boldsymbol{X}_{(i,j)}^{mp} - \boldsymbol{X}_{(i,m)}^{mp}\right)\right)\right|}{\left|\left(\boldsymbol{X}_{(i,j)}^{mp} - \boldsymbol{X}_{(i,l)}^{mp}\right) \times \left(\boldsymbol{X}_{(i,j)}^{mp} - \boldsymbol{X}_{(i,m)}^{mp}\right)\right|} & \text{plane points} \end{cases} \tag{19}$$

https://doi.org/10.5194/isprs-annals-X-4-2024-469-2024 | © Author(s) 2024. CC BY 4.0 License.

$$H_{i+1}=\frac{\partial f}{\partial X^{L}_{(i+1,i)}}\cdot\frac{\partial X^{L}_{(i+1,i)}}{\partial \delta x}=\begin{cases}\dfrac{\left\{\left[\left(\tilde{X}^{me}_{(i+1,i)}-X^{me}_{(i+1,i)}\right)\times\left(\tilde{X}^{me}_{(i+1,i)}-X^{mp}_{(i,l)}\right)\right]^{T}\right\}}{\left|\left(\tilde{X}^{me}_{(i+1,i)}-X^{me}_{(i+1,i)}\right)\times\left(\tilde{X}^{me}_{(i+1,i)}-X^{mp}_{(i,l)}\right)\right|}\cdot\left[\mathbf{R}^{i}_{i+1})(X^{mp}_{(i+1,i)})_{\times'} I\right]\\ \dfrac{\left\{\left[\left(X^{mp}_{(i,j)}-X^{mp}_{(i,l)}\right)\times\left(X^{mp}_{(i,j)}-X^{mp}_{(i,m)}\right)\right]^{T}\right\}}{\left|\left(\tilde{X}^{mp}_{(i,j)}-X^{mp}_{(i,l)}\right)\times\left(X^{mp}_{(i,j)}-X^{mp}_{(i,m)}\right)\right|}\cdot\left[\mathbf{R}^{i}_{i+1})(X^{mp}_{(i+1,i)})_{\times'} I\right]\end{cases} \tag{20}$$

Equation (19) where $\tilde{X}^{me}_{(i,i+1)}$ and $\tilde{X}^{mp}_{(i,i+1)}$ represent the coordinates of feature points in the edge point set F_{me} and the plane point set F_{mp}, respectively, after motion compensation and high-quality feature selection between the *i-th* frame and the *i-th+1* frame. Equation (20) where $\mathbf{R}^{i}_{i+1}$ represents the pose change of the LiDAR point cloud between the *i*-th frame and the *i-th+1* frame. $[\ ]_x$ denotes the skew-symmetric matrix transformation.

Solving for the updated state quantity $\breve{x}^{\alpha+1}_{i+1}$ and the Kalman gain K_{i+1} according to formulas (21) and (22):

$$\breve{x}^{\alpha+1}_{i+1}=\breve{x}^{\alpha}_{i+1}-K_{i+1}f^{\alpha}_{i+1}-\left(I-K_{i+1}H_{i+1}\right)\left(J^{\alpha}_{i+1}\right)^{-1}\left(\breve{x}^{\alpha}_{i+1}\ominus\breve{x}_{i+1}\right) \tag{21}$$

$$K_{i+1}=\left(\breve{P}^{-1}_{i+1}+H^{\mathrm{T}}_{i+1}L^{-1}_{i+1}H_{i+1}\right)^{-1}H^{\mathrm{T}}_{i+1}L^{-1}_{i+1} \tag{22}$$

Correct the pose and output the posterior state quantity $\hat{x}_{i+1}$ and the posterior covariance $\hat{P}_{i+1}$:

$$\hat{x}_{i+1}=\breve{x}^{\alpha+1}_{i} \tag{23}$$

$$\hat{P}_{i+1}=\left(I-K_{i+1}H_{i+1}\right)\breve{P}_{i+1} \tag{24}$$

(3)Keyframe-Submap Matching: To avoid redundant information in the output of the IESKF for IMU-LiDAR odometry frame by frame, keyframes are extracted for processing, while discarding the remaining data. Considering that the vehicle's motion state includes stationary states, keyframe selection is set based on the significant position change of the set of high-quality feature collections exceeding 1m. Based on the current keyframe pose, i nearest keyframes are selected to form an adjacent keyframe set $\{F_1,...,F_i\}$, the corresponding poses are subsequently transformed to the coordinate system of the current keyframe F, forming a local submap, which is continuously updated with changes in the motion state. The Levenberg-Marquardt (LM) registration algorithm is used in this paper to match keyframes with local submaps. The cost function $f\left(\bar{\boldsymbol{F}}_{i+1}\right)$ is established using the point-to-line distance d_{L} and point-to-plane distance d_{h} (referred to collectively as $\boldsymbol{d}$) between frames and submaps to solve for the optimal pose change relationship between frames and submaps:

$$\begin{cases}f\left(\bar{\boldsymbol{F}}_{i+1}\right)=\boldsymbol{d}\\ \boldsymbol{d}=\begin{bmatrix}d_{\mathrm{L}}\\ d_{\mathrm{h}}\end{bmatrix}\end{cases} \tag{25}$$

The optimal pose change relationship between frames is:

$$\begin{cases}\min\dfrac{1}{2}\left\|f\left(\bar{\boldsymbol{F}}_{i+1}\right)+\boldsymbol{J}\left(\bar{\boldsymbol{F}}_{i+1}\right)^{\mathrm{T}}\Delta\bar{\boldsymbol{F}}_{i+1}\right\|\\ \text{s.t.}\left\|\boldsymbol{D}\Delta\bar{\mathrm{F}}_{i+1}<\mu\right\|_{2}\end{cases} \tag{26}$$

In the equation, $\boldsymbol{J}$ represents the Jacobian matrix, $\boldsymbol{J}=\partial f/\partial\boldsymbol{F}_{i+1}$, where $\boldsymbol{D}$ is the coefficient matrix, and μ is the trust region radius.

Given the damping factor λ, the iterative derivation of the optimal estimate is as follows:

$$\boldsymbol{F}_{i+1}=\boldsymbol{F}_{i}-\left(\boldsymbol{J}_{i}^{\mathrm{T}}\boldsymbol{J}_{i}+\lambda diag\left(\boldsymbol{J}_{i}^{\mathrm{T}}\boldsymbol{J}_{i}\right)\right)^{-1}\boldsymbol{J}_{i}^{\mathrm{T}}\boldsymbol{d} \tag{27}$$

Iterate continuously until convergence is achieved, obtaining the current pose estimate $\boldsymbol{T}_{i+1}=\bar{\boldsymbol{T}}_{i+1}$, The relative pose change between two adjacent keyframes is:

$$\Delta\boldsymbol{F}_{i,i+1}=\boldsymbol{F}_{i}^{-1}\boldsymbol{F}_{i+1} \tag{28}$$

2.4 Factor Graph Optimization Pose Model

Utilizing the factor graph model computed by the front-end, residual calculation is performed and global optimization is conducted. The constraint relations in this paper are composed of three types of graph models: IMU pre-integration factors, LiDAR-inertial odometry factors, Loop closure detection factors and Odometry factors. The optimization objective term for relative pose between adjacent frames is:

$$\phi_{L}(\boldsymbol{x})=\frac{1}{2}\left\|r\left(\boldsymbol{x}_{i},\boldsymbol{x}_{i+1}\right)\right\|^{2}_{\Sigma} \tag{29}$$

where $\boldsymbol{x}$ representing the state to be optimized; r denoting the residual of the relative pose factor; $\boldsymbol{x}_i,\boldsymbol{x}_{i+1}$ respectively representing the motion states at time i and $i+1$; and Σ which represents the covariance matrix of the constraint uncertainty.

2.4.1 IMU Pre-integration Factors: The high-frequency pre-integration of IMU data between adjacent keyframes reduces the computational burden of multiple iterations while imposing constraints on IMU motion. These constraints are jointly optimized with other constraints to obtain the final pose estimation. The measurements from the accelerometer and gyroscope in the IMU are as follows:

$$\hat{\omega}_{\mathrm{t}}=\omega_{t}+b^{\omega}_{t}+n^{\omega}_{t} \tag{30}$$

$$\hat{a}_{t}=\mathbf{R}^{IW}_{t}\left(a_{t}-g\right)+b^{a}_{t}+n^{a}_{t} \tag{31}$$

Where $\hat{\omega}_{\mathrm{t}}$ and $\hat{a}_t$ are the measurements of the IMU in its own coordinate system I at time t, influenced by the transformation biases b_t and white noise n_t, $\mathbf{R}^{IW}_{t}$ is the rotation matrix from the IMU coordinate system I to the world coordinate system W, and g is the constant gravitational acceleration in the W coordinate system.

The vehicle's velocity and attitude at time Δt are derived from the measurements:

$$v_{t+\Delta t}=v_{t}+g\Delta t+\mathbf{R}_{t}\left(\hat{a}_{t}-b^{a}_{t}-n^{a}_{t}\right)\Delta t \tag{32}$$

$$p_{t+\Delta t}=p_{t}+v_{t}\Delta t+\frac{1}{2}g\Delta t^{2}+\frac{1}{2}\mathbf{R}_{t}\left(\hat{a}_{t}-b^{a}_{t}-n^{a}_{t}\right)\Delta t^{2} \tag{33}$$

$$\mathbf{R}_{t+\Delta t}=\mathbf{R}_{t}\exp\left(\left(\hat{\omega}_{t}-b^{\omega}_{t}-n^{\omega}_{t}\right)\Delta t\right) \tag{34}$$

Define the rotation matrix as $\mathbf{R}=\mathbf{R}^{WI}_{t}=\mathbf{R}^{IWT}_{t}\mathbf{R}^{IW}_{t}$ .Assuming constant angular velocity and acceleration during the integration process, according to the differential equation in equation (6), integrate to compute the IMU data between the *i-th* and *i+1-th* frames, obtaining the IMU state update equation for the *i+1-th* frame:

$$\begin{bmatrix} p_{i+1}^{W} \\ v_{i+1}^{W} \\ q_{i+1}^{W} \\ b_{i+1}^{a} \\ b_{i+1}^{g} \end{bmatrix} = \begin{bmatrix} p_i^{\mathrm{W}} + v_i^{\mathrm{W}}\Delta \mathrm{t} - \frac{1}{2}\mathrm{g}^{\mathrm{W}}\Delta \mathrm{t}^2 + q_i^{\mathrm{W}}\left(\alpha_i^{\mathrm{I}} + \beta_i^{\mathrm{I}}\Delta \mathrm{t} + \frac{1}{2}\bar{\mathrm{a}}_i\Delta \mathrm{t}^2\right) \\ v_i^{\mathrm{W}} - \mathrm{g}^{\mathrm{W}}\Delta \mathrm{t} + \mathrm{q}_i^{\mathrm{W}}\left(\beta_i^{\mathrm{I}} + \bar{\mathrm{a}}_i\Delta \mathrm{t}\right) \\ \mathrm{q}_i^{\mathrm{w}}\left(\mathrm{q}_i^{\mathrm{I}} \otimes \begin{bmatrix} 1 \\ \frac{1}{2}\bar{\omega}_i\Delta \mathrm{t} \end{bmatrix}\right) \\ b_i^{\mathrm{a}} \\ \mathrm{b}_{\mathrm{j}}^{\mathrm{g}} \end{bmatrix} \tag{35}$$

2.4.2 Laser-Inertial Odometry Factor: In order to obtain a more accurate pose transformation between two keyframes, the relative pose constraint relationship between LiDAR keyframes is utilized to optimize together with the IMU pre-integration factors in the sliding window.

$$r_L = \begin{bmatrix} \Delta t - \mathbf{R}_i^{\mathrm{T}}\left(t_{i+1} - t_i\right) \\ \log\left(\Delta \mathbf{R}^{\mathrm{T}}\mathbf{R}_i^{\mathrm{T}}\mathbf{R}_{i+1}\right) \end{bmatrix} \tag{36}$$

where $\mathbf{R}$ represents the rotation matrix in the Laser-Inertial Odometry.

2.4.3 Loop Detection Factor: In this paper, the method for loop detection adopts the keyframe-based Euclidean distance detection method proposed in LIO-SAM (Ye et al., 2019). Considering the short distance between adjacent keyframes of vehicle motion, to avoid redundant loop detections, odometer data is utilized to judge loops. Based on the translation information of keyframes, other keyframes within a 15-meter range and with time intervals greater than 30 seconds from adjacent keyframes are searched. After accumulating a certain number of waiting keyframes, historical keyframes that meet the conditions are identified for loop detection. Utilizing keyframes satisfying the conditions before and after the loop frame, a local map of the loop frame is constructed for frame-to-map matching. The relative pose change factor is solved through equation (28), and loop constraints are added for global error optimization to determine the optimal pose.

3. Experiments And Analysis

The experiments in this paper were conducted in one university underground parking. The wheeled mobile robot test platform was equipped with a Velodyne-16 LiDAR, operating at a sampling frequency of 10 Hz; the IMU used was the laboratory-developed Inertial-aided Pedestrian Navigation Module (IPMV), with a sampling frequency of 100Hz. The experimental site and the test platform are shown in Figure 4. There are various elements in the environment, such as speed bumps, drains, and uneven roads, which allow for testing the positioning accuracy and robustness of the algorithms.

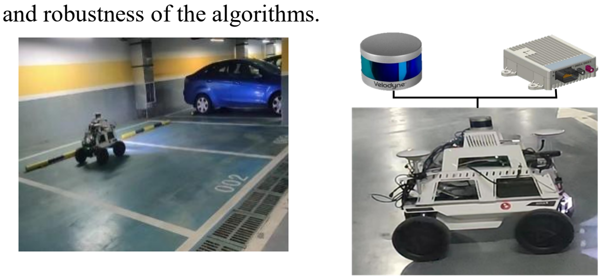

(a) The Underground Parking (b) The wheeled mobile robot

Figure 4. Underground Garage Test Environment and Experimental Platform.

For the purpose of simulating underground parking garage localization experiments, three parking spaces were randomly selected within the garage. The experimental routes were configured as follows: Route1: entrance to parking spaces A, B, C, and then to the exit; Route2: vehicles parking in spaces A, B, C; Route3: from the entrance, reversing to the exit. The driving route map and localization results are shown in Figures 5-6.

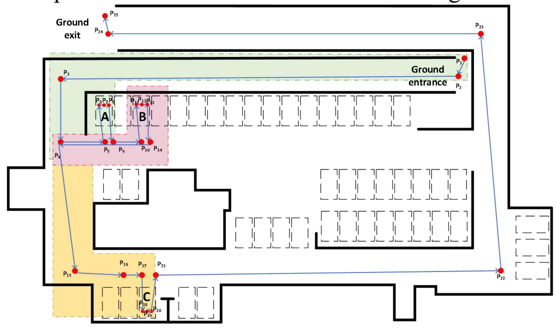

(a) The plan view of the driving route.

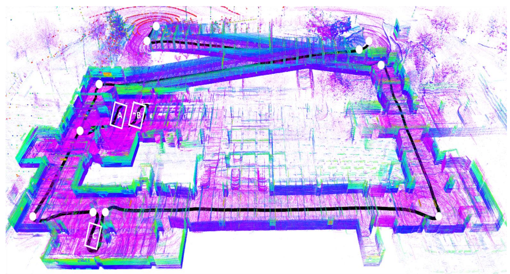

(b) Side view of the point cloud map.

Figure 5. Route Map.

Compared with traditional LiDAR SLAM algorithms such as A-LOAM (Ji et al., 2014), LeGO-LOAM (Shan and Englot, 2018), LIO-SAM (Meyers et al., 2020), and FAST-LIO2 (Xu et al., 2021) as illustrated in Figure 6.

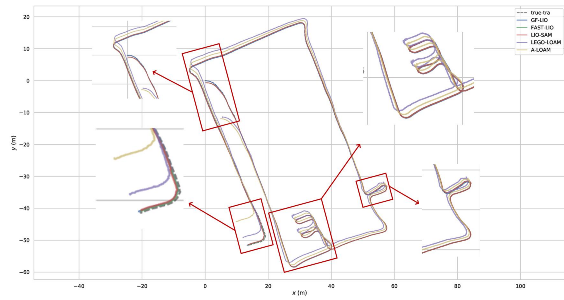

(a) Localization results for Route1.

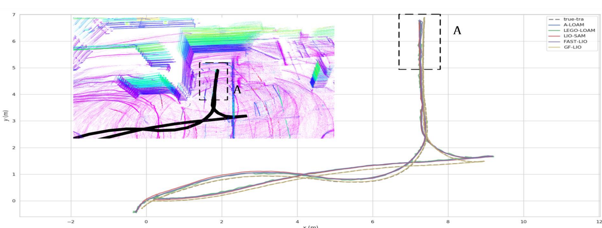

(

b) Localization results for Route2- Garage A.

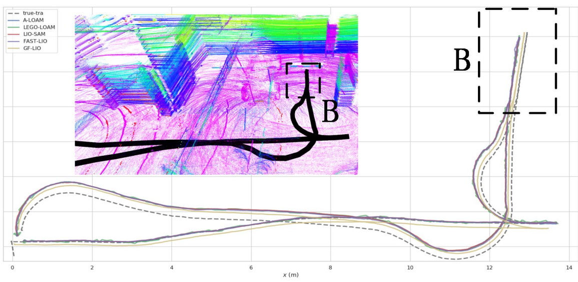

(c) Localization results for Route2- Garage B.

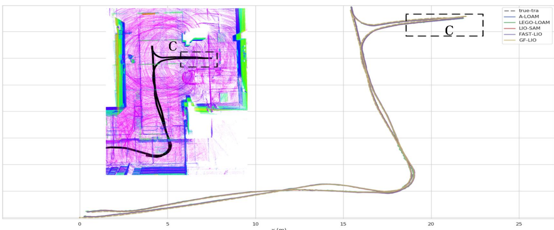

(d) Localization results for Route2-Garage C.

(e) Localization results for Route3.

Figure 6. Localization results in the underground parking garage scene.

As shown in Figure 6, all five algorithms closely align with the ground truth trajectory. The red box marks the starting and ending positions of the vehicle, as well as its turning trajectory. However, A-LOAM and LEGO-LOAM, lacking IMU pre-integration, exhibit larger errors. In autonomous parking scenarios, vehicles often require significant turning movements within a short period, emphasizing the importance of improving turning localization accuracy. During turning manoeuvres, GF-LIO utilizes loop closure detection for pose optimization, resulting in trajectories that closely follow the actual route. The loop closure detection in experiments A, B, and C in the parking garage is depicted in Figure 7.

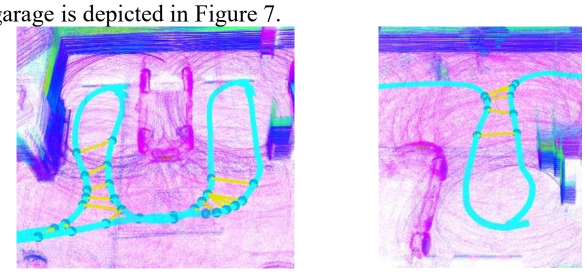

Figure 7. Loop Closure Detection in Parking Garage Localization

The mean squared error comparison of the localization results for all routes between GF-LIO and traditional algorithms is presented in Table 1.

Route	Algorithm	△ x	△ y	△ z	Level Error	Total Error
Route1 (Length: 348.727m ; Time: 674.347s)	A-LOAM	0.46	0.68	0.35	0.82	0.90
	LEGO-LOAM	0.55	0.73	0.34	0.91	0.97
	LIO-SAM	0.27	0.69	0.16	0.74	0.76
	FAST-LIO	0.26	0.68	0.15	0.73	0.74
	GF-LIO	**0.20**	**0.62**	**0.09**	**0.65**	**0.65**
Route2 -Garage A (Length: 348.727m; Time: 674.347s)	A-LOAM	0.27	0.16	0.41	0.34	0.51
	LEGO-LOAM	0.34	0.25	0.50	0.42	0.65
	LIO-SAM	0.27	0.22	0.15	0.35	0.38
	FAST-LIO	0.24	0.19	0.08	0.31	0.32
	GF-LIO	**0.14**	**0.16**	**0.09**	**0.21**	**0.23**
Route2 -Garage B (Length: 348.727m; Time: 674.347s)	A-LOAM	0.27	0.16	0.41	0.32	0.52
	LEGO-LOAM	0.34	0.25	0.50	0.42	0.65
	LIO-SAM	0.27	0.14	0.03	0.30	0.30
	FAST-LIO	0.18	0.21	0.08	0.27	0.29
	GF-LIO	**0.14**	**0.16**	**0.09**	**0.21**	**0.23**
Route2 -Garage C (Length: 348.727m; Time: 674.347s)	A-LOAM	0.34	0.12	0.03	0.36	0.37
	LEGO-LOAM	0.47	0.29	0.07	0.55	0.55
	LIO-SAM	0.24	0.11	0.03	0.26	0.26
	FAST-LIO	0.22	0.11	0.02	0.24	0.24
	GF-LIO	**0.12**	**0.16**	**0.01**	**0.20**	**0.20**
Route3 (Length: 348.727m; Time: 674.347s)	A-LOAM	0.37	0.13	0.10	0.36	0.41
	LEGO-LOAM	0.57	0.29	0.03	0.48	0.64
	LIO-SAM	0.36	0.13	0.02	0.26	0.38
	FAST-LIO	0.25	0.14	0.04	0.24	0.29
	GF-LIO	**0.17**	**0.16**	**0.07**	**0.20**	**0.24**

Table 1. Localization Results Comparison in Underground Parking Garage Scenarios. (RMSE: meters (m))

Drawing from the results of five experimental trials, the following observations can be made regarding the performance of the algorithm introduced in this study, GF-LIO, which is specifically designed for navigating environments within underground parking garages:

1. GF-LIO leverages an optimized fusion of LiDAR and IMU data through a factor graph approach, enabling the precise extraction of both planar features, such as walls and doors, and ground features, including parking bumpers and stationary vehicles. This leads to the generation of a detailed and comprehensive point cloud map of the underground parking garage environment.

2. The algorithm demonstrates a significant reduction in root mean square errors (RMSE) in both the horizontal and vertical planes when compared to traditional methods. More specifically, GF-LIO enhances positioning accuracy by 27.22%, 33.07%, 13.98%, and 12.53% respectively for Route 1; by 54.75%, 64.41%, 38.83%, and 26.48% respectively for Route 2 - Garage A; by 56.29%, 65.29%, 25.35%, and 20.95% respectively for Route 2 - Garage B; by 45.19%, 63.78%, 23.61%, and 18.03% respectively for Route 2 - Garage C; and by 40.15%, 61.71%, 36.32%, and 15.84% respectively for Route 2 overall. It is noteworthy that Route 2, which involves entry experiments in different garages over shorter distances, yields a higher number

of loop closures during the entry and exit phases, contributing to the notably enhanced accuracy. Routes 1 and 3 include sections where the vehicle enters and exits the garage, presenting substantial variations along the z-axis. Additionally, the segment from P22 to P23 encompasses speed bumps and ramps, as indicated by the relative error change plot for Route 1 in Figure 8, where an observable increase in error is noted for the P22 to exit segment.

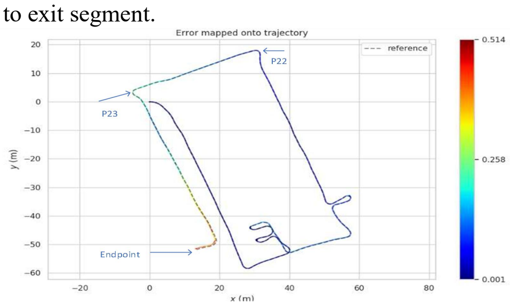

Figure 8. Relative Error Variation Plot for Route 1.

4. Conclusion

This study addresses the challenge of GNSS signal unavailability in subterranean parking facilities by introducing a novel model known as GF-LIO. This model integrates the IESKF (Interactive Extended State Kalman Filter) with a factor graph for a tightly-coupled fusion of LiDAR and IMU data.GF-LIO model capitalizes on the rich environmental features for map matching to ascertain the relative pose of the LiDAR with precision, establishes an IESKF-driven LiDAR-inertial odometry system, and exploits IMU pre-integration and loop closure detection factors to enforce a unified constraint. Through the optimization of the factor graph, GF-LIO achieves a tight integration of LiDAR and IMU. Field entry tests in underground parking lots have shown that GF-LIO provides enhanced localization outcomes in structured settings. In the context of underground environments that present substantial challenges such as sharp turns and uneven surfaces, including speed bumps, GF-LIO surpasses conventional laser SLAM techniques in both accuracy and robustness. This model exhibits superior adaptability for the localization and mapping of mobile robots in intricate underground scenarios.

Acknowledgements

This research was supported by the National Natural Science Foundation of China (No.42374024), and the Beijing Natural Science Foundation General Program (No. 8222011).

References

Ahmed, El-Mowafy, et al., 2018: Integrity monitoring for Positioning of intelligent transport systems using integrated RTK-GNSS, IMU and vehicle odometer. *Iet Intelligent Transport Systems*. doi: 10.1049/iet-its.2018.0106.

Faragher,R., Harle,R., 2015: Location Fingerprinting With Bluetooth Low Energy Beacons. *IEEE Journal on Selected Areas in Communications*, 33(11), 2418-2428. doi: 10.1109/JSAC.2015.2430281.

Han,J., Kim,J., et al., 2018: Precise Localization and Mapping in Indoor Parking Structures via Parameterized SLAM. *IEEE Transactions on Intelligent Transportation Systems*, 19(12),1-12. doi: 10.1109/TITS.2018.2885341.

Kaess,M., Johannsson,H., et al., 2011: iSAM2: Incremental smoothing and mapping with fluid relinearization and incremental variable reordering. *2011 IEEE International Conference on Robotics and Automation (ICRA)*. doi: 10.1109/ICRA.2011.5979641.

Li,B., Yang,L., et al., 2018: Collaborative Mapping and Autonomous Parking for Multi-Story Parking Garage. *IEEE Transactions on Intelligent Transportation Systems*, 19(12), 1629-1639. doi:10.1109/TITS.2018.2791430.

Li,Z., Dehaene,W., et al., 2009: A 3-tier UWB-based indoor localization system for ultra-low-power sensor networks. *IEEE Transactions on Wireless Communications*, 8(6), 2813-2818. doi: 10.1109/TWC.2009.080602.

Li,Y., Feng,F., et al., 2024: Localization for Intelligent Vehicles in Underground Car Parks Based on Semantic Information. *IEEE Transactions on Intelligent Transportation Systems*, 25(2), 1317-1332. doi: 10.1109/TITS.2023.3320088.

Lategahn,H., Stiller,C., 2014: Vision-Only Localization. *IEEE Transactions on Intelligent Transportation Systems,* 15(3), 1246-1257. doi: 10.1109/TITS.2014.2298492.

Meyers,D., Englot,B., et al., 2020: LIO-SAM: Tightly-coupled Lidar Inertial Odometry via Smoothing and Mapping. *Journal of Advances in Robotics & Its Surgical Applications*, doi: 10.1109/IROS45743.2020.9341176.

Qin,C., Ye,H., et al., 2020: LINS: A Lidar-Inertial State Estimator for Robust and Efficient Navigation. In *Proc. IEEE Int. Conf. Robot. Autom. (ICRA)*, Paris, France, 2020, pp. 8899-8906. doi:10.1109/ICRA40945.2020.9197567.

Shan,T., Englot,B., 2018. LeGO-LOAM: Lightweight and Ground-Optimized Lidar Odometry and Mapping on Variable Terrain. In *Proc. IEEE/RSJ Int. Conf. Intell. Robots Syst. (IROS)*, Madrid, Spain, pp. 4758-4765. doi:10.1109/IROS.2018.8594299.

Xu,W., Cai,Y., et al., 2022: FAST-LIO2: Fast Direct LiDAR-Inertial Odometry. *IEEE Trans. Robot.*, vol. 38, no. 4, pp. 2053-2073, Aug. 2022, doi: 10.1109/TRO.2022.3141876.

Yan,Y., Hang,Y., et al., 2021: Visual SLAM in Long-Range Autonomous Parking Application Based on Instance-Aware Semantic Segmentation via Multi-Task Network Cascades and Metric Learning Scheme. *SAE International Journal of Advances and Current Practices in Mobility*, 3(3), 1357-1368. doi: 10.4271/2021-01-0077.

Yang,C., Shao,H.R., 2015: WiFi-based indoor positioning. *IEEE Commun. Mag.*, vol. 53, no. 3, pp. 150-157, Mar. 2015, doi: 10.1109/MCOM.2015.7060497.

Ye,H., Chen,Y., et al., 2019: Tightly Coupled 3D Lidar Inertial Odometry and Mapping. In *Proc. IEEE Int. Conf. Robot. Autom. (ICRA)*, Montreal, QC, Canada, 2019, pp. 3144-3150. doi:10.1109/ICRA.2019.8793511.

Zhang,J.; Singh,S., 2014. LOAM: Lidar Odometry and Mapping in Real-time. In *Proc. Robotics: Sci. Syst. Conf.*, pp. X-007. doi: 10.15607/RSS.2014.X.007.